ACS NANO

Subscriber access provided by Oregon State University

Article

NbSiTe: A Stable Narrow-Gap Two-Dimensional Material with Ambipolar Transport and Mid-Infrared Response

Mingxing Zhao, Wei Xia, Yang Wang, Man Luo, Zhen Tian, Yanfeng Guo, Weida Hu, and Jiamin Xue

ACS Nano, **Just Accepted Manuscript** • Publication Date (Web): 30 Aug 2019

Downloaded from pubs.acs.org on August 30, 2019

Just Accepted

"Just Accepted" manuscripts have been peer-reviewed and accepted for publication. They are posted online prior to technical editing, formatting for publication and author proofing. The American Chemical Society provides "Just Accepted" as a service to the research community to expedite the dissemination of scientific material as soon as possible after acceptance. "Just Accepted" manuscripts appear in full in PDF format accompanied by an HTML abstract. "Just Accepted" manuscripts have been fully peer reviewed, but should not be considered the official version of record. They are citable by the Digital Object Identifier (DOI®). "Just Accepted" is an optional service offered to authors. Therefore, the "Just Accepted" Web site may not include all articles that will be published in the journal. After a manuscript is technically edited and formatted, it will be removed from the "Just Accepted" Web site and published as an ASAP article. Note that technical editing may introduce minor changes to the manuscript text and/or graphics which could affect content, and all legal disclaimers and ethical guidelines that apply to the journal pertain. ACS cannot be held responsible for errors or consequences arising from the use of information contained in these "Just Accepted" manuscripts.

is published by the American Chemical Society. 1155 Sixteenth Street N.W., Washington, DC 20036
Published by American Chemical Society. Copyright © American Chemical Society. However, no copyright claim is made to original U.S. Government works, or works produced by employees of any Commonwealth realm Crown government in the course of their duties.

1
2
3
4
5
6
7
8
9
10
11
12
13
14
15
16
17
18
19
20
21
22
23
24
25
26
27
28
29
30
31
32
33
34
35
36
37
38
39
40
41
42
43
44
45
46
47
48
49
50
51
52
53
54
55
56
57
58
59
60

Nb_2SiTe_4: A Stable Narrow-Gap Two-Dimensional Material with Ambipolar Transport and Mid-Infrared Response

Mingxing Zhao,[†,§,⊥,‖] Wei Xia,[†,⊥,‖] Yang Wang,[‡] Man Luo,[‡] Zhen Tian,[†] Yanfeng Guo[†*], Weida Hu[‡*] and Jiamin Xue[†*]

[†]School of Physical Science and Technology, ShanghaiTech University, Shanghai 201210, China

[‡]State Key Laboratory of Infrared Physics, Shanghai Institute of Technical Physics, Chinese Academy of Sciences, Shanghai 200083, China

[§]Shanghai Institute of Ceramics, Chinese Academy of Sciences, Shanghai 200050, China

[⊥]University of Chinese Academy of Sciences, Beijing 100190, China

ABSTRACT

Two-dimensional (2D) materials with narrow band gaps (~ 0.3 eV) are of great importance for realizing ambipolar transistors and mid-infrared (MIR) detections. However, most of the 2D materials studied to date have band gaps that are too large. A few of the materials with suitable band gaps are not stable under ambient conditions. In this study, the layered Nb_2SiTe_4 is shown

1
2
3
4
5
6
7
8
9
10
11
12
13
14
15
16
17
18
19
20
21
22
23
24
25
26
27
28
29
30
31
32
33
34
35
36
37
38
39
40
41
42
43
44
45
46
47
48
49
50
51
52
53
54
55
56
57
58
59
60

to be a stable 2D material with a band gap of 0.39 eV. Field-effect transistors based on few-layer Nb_2SiTe_4 show ambipolar transport with similar magnitude of electron and hole current and high charge-carrier mobility of ~ 100 $cm^2V^{-1}s^{-1}$ at room temperature. Optoelectronic measurements of the devices show clear response to an MIR wavelength of 3.1 μm with a high responsivity of ~ 0.66 AW^{-1}. These results establish Nb_2SiTe_4 as a good candidate for ambipolar devices and MIR detection.

KEYWORDS: Nb_2SiTe_4, ambipolar transistor, mid-infrared, two-dimensional material, narrow gap, stability

Materials with narrow band gaps in the range of 0.15 eV to 0.4 eV are important in the family of semiconductors for their applications in mid-infrared (MIR) detections. Among them, indium arsenide, mercury cadmium telluride and so on are the most studied and used materials. In addition to these conventional semiconductors, newly developed narrow-gap two-dimensional (2D) materials are also showing great potential in the MIR detections. For example, few-layer black phosphorus (bP) with a band gap of ~ 0.3 eV has been used to demonstrate high photo responsivity and detectivity in the MIR range.[1-3] When alloyed with arsenide, the band gap of black arsenic phosphorus (bAP) can be further tuned from ~ 0.3 eV to ~ 0.15 eV, which extends the spectrum to the long-wavelength infrared.[4,5] The layered nature of these materials gives them large flexibility and ease of integration with other materials to form various device structures.[3,6,7]

In addition to their applications in optoelectronics, narrow-gap 2D semiconductors such as bP can be used as the channel material of field-effect transistors (FET) and support ambipolar

transport, in which the majority carriers of the channel can be easily switched between electrons and holes by electrostatic doping of the gate voltage.[8,9] This property offers great opportunity for device functions such as field-programmable p-n junctions,[10] which are not achievable by conventional semiconductors.

Due to these applications, narrow-gap 2D materials are in high demand. However, most of the 2D semiconductors studied to date have band gaps in the order of 1 eV or higher.[11] bP and bAP have suitable band gaps, but these materials degrade within hours under ambient condition due to the chemical instability of phosphorus.[4,12,13] Thus, more stable narrow-gap 2D materials are needed. Herein, we report a layered material Nb_2SiTe_4 (NST) with a band gap of 0.39 eV. When few-layer NST is fabricated into an FET, it shows ambipolar transport with similar capability of conducting electrons and holes. A respectable hole mobility of ~ 100 $cm^2V^{-1}s^{-1}$ at room temperature is obtained. When illuminated by MIR light with a wavelength of 3.1 μm, NST devices demonstrate high photo responsivity of ~ 0.66 AW^{-1}. They also show good stability under ambient conditions without any encapsulation. These findings demonstrate NST to be a stable narrow-gap 2D material with great application potentials.

RESULTS AND DISCUSSION

1
2
3
4
5
6
7
8
9
10
11
12
13
14
15
16
17
18
19
20
21
22
23
24
25
26
27
28
29
30
31
32
33
34
35
36
37
38
39
40
41
42
43
44
45
46
47
48
49
50
51
52
53
54
55
56
57
58
59
60

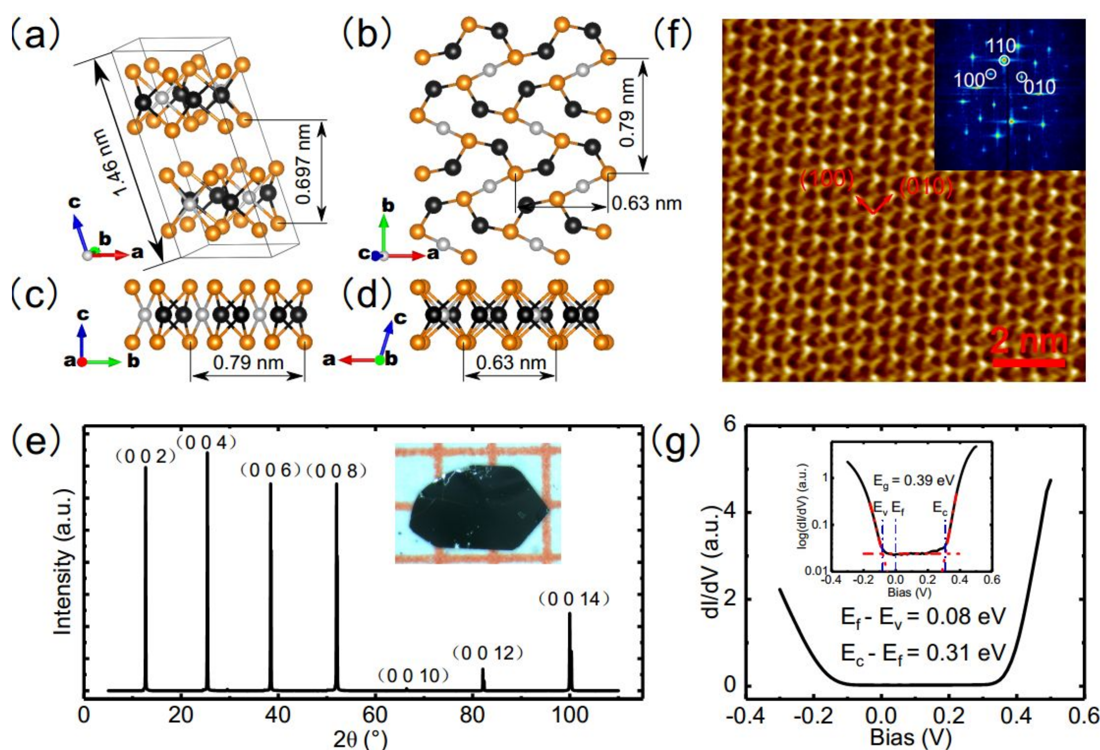

Figure 1. (a) Perspective view of few-layer NST showing atoms of Te (gold), Nb (black), and Si (gray). (b) Top view and (c), (d) side views of monolayer NST. (e) XRD data of NST. The X-ray source is Cu Kα line with the wave length of 0.154 nm. Inset: optical image of a bulk NST crystal. (f) Atomically resolved image of an NST crystal measured by STM with the corresponding fast Fourier transform in the inset. STM parameters: V = 0.5 V, I = 100 pA. (g) The dI/dV spectra of an NST crystal. Inset is the same data plotted in log scale for a better determination of band edges. The band gap E_g is measured to be 0.39 eV. STS parameters: $V_{initial}$ = 0.5 V, $I_{initial}$ = 100 pA; lock-in frequency f = 991.2 Hz, modulation voltage V_{rms} = 10 mV.

NST was synthesized decades ago,[14] but there have been few studies about it. Bulk NST crystal belongs to the space group of *P121/c1* (No. 14),[15] which is in the monoclinic crystal system. Figure 1a to 1d show the different views of the NST structure (more 3D views can be found in Figure S1 of the Supporting Information, SI). It is a layered material formed by stacking the Te-

(Nb, Si)-Te sandwich layers, which bears similarity to the transitional metal dichalcogenides (TMDs) such as MoS_2,[16] $NbSe_2$[17] and so on. The inner atomic layer consists of two types of atoms (Nb and Si) instead of one in the TMDs. The lattice parameters have been determined as a = 0.63 nm, b = 0.79 nm, c = 1.47 nm, α = 90°, β = 107°, and γ = 90°.[15] We synthesized the NST crystals with self-flux method (see the Experimental section). The as grown crystals were black, thin flakes with metal luster, and their size was measured in millimeters (inset of Figure 1e). Due to the layered nature, powder X-ray diffraction (XRD) was used to probe the basal planes in the crystal. Sharp Bragg peaks indicated the high quality of our crystals. According to the Bragg's law, $2\mathrm{d}\sin\theta = n\lambda$, where d is the layer distance, θ is the X -ray incident angle, n is the order of a Bragg peak, and $\lambda = 0.154$ nm, the wavelength of the X-ray. For the first peak in Figure 1e, $\theta = 6.34°$ and $n = 1$, which gives d to be 0.697 nm. For this monoclinic crystal structure, the c axis forms an angle of 107° with the basal plane and the unit cell contains two layers. Hence, $\mathrm{c} = 2\mathrm{d}/\sin 107° = 1.46$ nm. To complement the XRD study, we used scanning tunneling microscopy (STM) which resolves the atomic structure within the basal plane (Figure 1f). The orthorhombic structure was clearly visible with lattice constants of 0.63 nm and 0.78 nm; these findings are consistent with values found in the literature.[15] Figure 1b and 1f show that the unit cell of NST contains a large number of atoms, which resulted in many phonon modes as shown by Raman spectroscopy (Figure S2 in the SI). In addition to revealing the atomic structure, more importantly, STM can be used to measure the band structure with the technique of scanning tunneling spectroscopy (STS).[18,19] In Figure 1g, The Fermi level is located at 0.08 eV above the valence band edge E_v, indicating the intrinsic p-type doping. The band gap E_g was determined to be 0.39 eV in the MIR range, which is promising for both ambipolar transport and MIR detection.

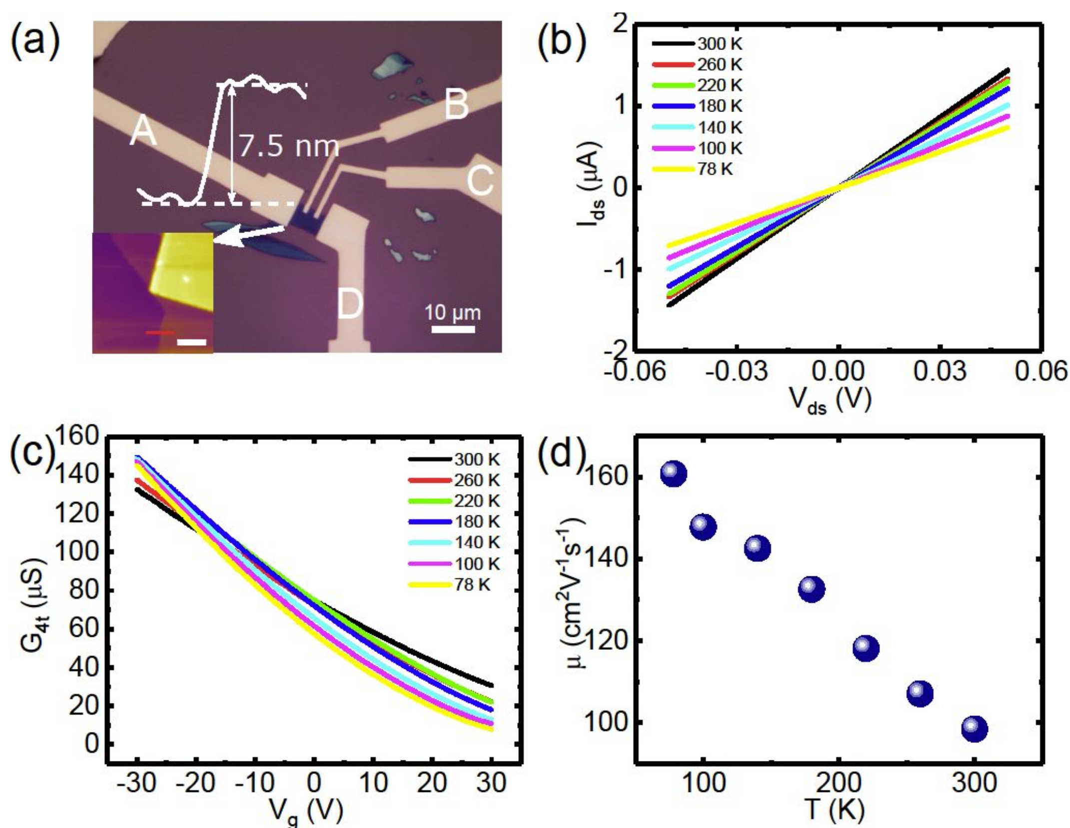

Figure 2. (a) The optical image of the few-layer NST device with the height profile of the channel along the white line. Inset: the AFM image of one part of the device. The red line marks the position where the height profile was taken. The inset scale bar was 2 μm. (b) Drain-source current I_{ds} between electrodes A and D *versus* V_{ds} at different temperatures. (c) Four-probe conductance (G_{4t}) as a function of back-gate voltage (V_g) at various temperatures. (d) Four-probe hole mobility as a function of temperature extracted from (c).

To measure the transport property of few-layer NST, scotch tape method was adopted to exfoliate NST onto highly p-doped Si substrate covered with 300 nm thermally grown SiO_2. Then, electron-beam lithography and metal deposition were used to fabricate the device. A typical FET device is shown in the optical image of Figure 2a. The flake thickness was measured

1
2
3
4
5
6
7
8
9
10
11
12
13
14
15
16
17
18
19
20
21
22
23
24
25
26
27
28
29
30
31
32
33
34
35
36
37
38
39
40
41
42
43
44
45
46
47
48
49
50
51
52
53
54
55
56
57
58
59
60

by atomic force microscope (AFM) to be 7.5 nm (other thicknesses of few-layer NST showed similar behavior). The metal electrodes consisted of 10 nm of Ti and 40 nm of Au. All transport measurements were performed in vacuum (~10^{-5} mbar) and in dark with a Janis ST-500 probe station.

The linear two-terminal output curves measured from 300 K to 78 K (Figure 2b) indicated that Ti forms good contacts with NST. We determined the work function of NST to be 4.36 eV by ultraviolet photoelectron spectroscopy (Figure S3), which matched well with that of Ti (4.3 eV).[20] To extract the intrinsic field-effect mobility, four-terminal transfer curves were measured as a function of temperature (Figure 2c). The p-type transport was consistent with the band structure measured by STS in Figure 1g. Mobility μ was calculated by $= \frac{L}{WC_{ox}} \frac{\mathrm{d}G}{\mathrm{d}V_g}$, where G is the conductance, V_g is the back-gate voltage, $C_{ox} = 1.15 \times 10^{-8}\,\mathrm{F\,cm^{-2}}$ is the specific capacitance of gate oxide, and L (W) is the length (width) of the channel. The mobility at room temperature was 98 $\mathrm{cm^2V^{-1}s^{-1}}$ and it increased as the temperature was lowered, reaching 160 $\mathrm{cm^2V^{-1}s^{-1}}$ at 78 K (Figure 2d). Compared with the majority of 2D materials, NST has a higher mobility,[21,22] which is essential for high performance electronic devices. Similar transport properties were obtained on 8 other devices (see Figure S4 for data of two other devices), although some variations in the transport properties such as mobility and threshold voltage existed among them. With device optimization, such as better substrates and dielectric screening,[23,24] the mobility should be further improved.

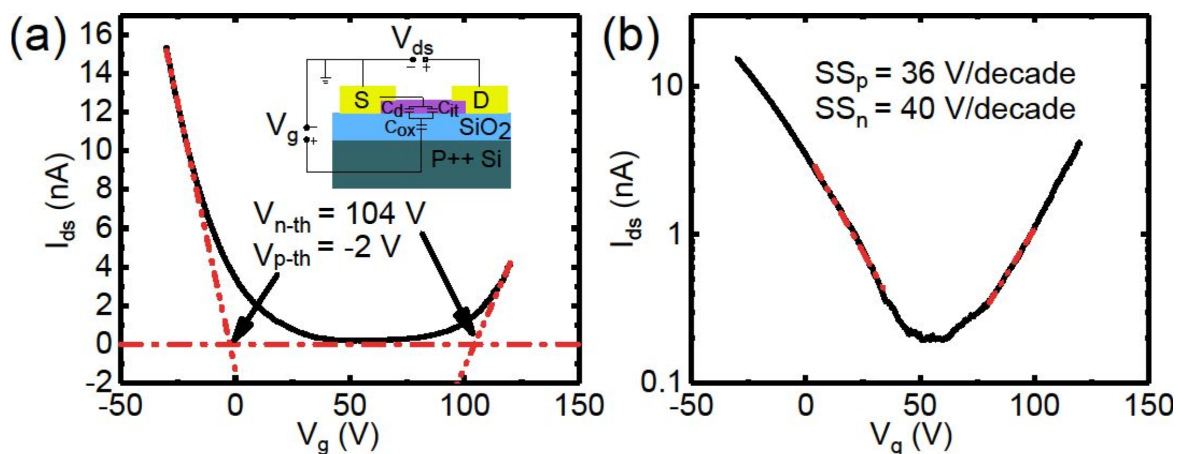

Figure 3. (a) Transfer curve of an NST device showing ambipolar transport. $V_{n\text{-th}}$ and $V_{p\text{-th}}$ represent the threshold voltages on the electron side and hole side, respectively. Inset: schematic of equivalent capacitance model of the device. C_d and C_{it} represent the depletion layer capacitance and interface capacitance, respectively. (b) Data from (a) plotted in log scale. Red lines are the linear fitting curves to extract the subthreshold swings of the electron side (SS_n) and hole side (SS_p).

Due to the narrow band gap, it is possible to change the majority carrier type in the channel from holes to electrons simply by the back-gate voltage. Figure 3a shows the transfer curve of a 5.7 nm NST FET (Figure S5), where ambipolar behavior can be clearly seen. The electron and hole currents have comparable magnitude, indicating similar Schottky barrier heights between Ti and the conduction and valence bands of NST. Previously reported narrow-gap 2D materials such as bP can also support ambipolar transport,[8,9] but the electron current is usually orders of magnitude lower than the hole current, which undermines the tunability of a device.

Further analysis of the data in Figure 3a can be used to extract the transport gap, which is given by[25]

$$E_g = e\left(V_{ds} + \left(\frac{V_{n-th}}{\beta_n} - \frac{V_{p-th}}{\beta_p}\right)\right), \quad (1)$$

where e is the electron charge, V_{ds} is the source-drain bias (100 mV in Figure 3a), V_{n-th} (V_{p-th}) is the threshold voltage on the electron (hole) side, and β_n (β_p) is the gate efficiency in tuning the band edge on the electron (hole) side, which is defined below. The threshold voltages are determined from Figure 3a. The subthreshold swing (SS) of an FET can be written as[26]

$$SS = \ln 10 \frac{kT}{e}\left(1 + \frac{C_d + C_{it}}{C_{ox}}\right) \equiv \ln 10 \frac{kT}{e}\beta, \quad (2)$$

where k is the Boltzmann constant, T is the temperature (150 K in our case), and C_d (C_{it}) is the depletion (interface) capacitance. The gate efficiency β is defined as $\beta = 1 + \frac{C_d + C_{it}}{C_{ox}}$. The equivalent capacitance circuit is shown in the inset of Figure 3a. Due to the presence of C_d and C_{it}, the gate voltage V_g in the subthreshold regime can only cause a down scaled shift of the bands in the device. The scaling factor β can be extracted from the fittings in Figure 3b. Since the electron side and hole side showed slightly different SS, both values were used in Equation 1. The calculated transport gap of NST was 0.18 eV, less than the STS value. This difference may have come from the thermal broadening of the band edges and the nonuniform doping in the device.

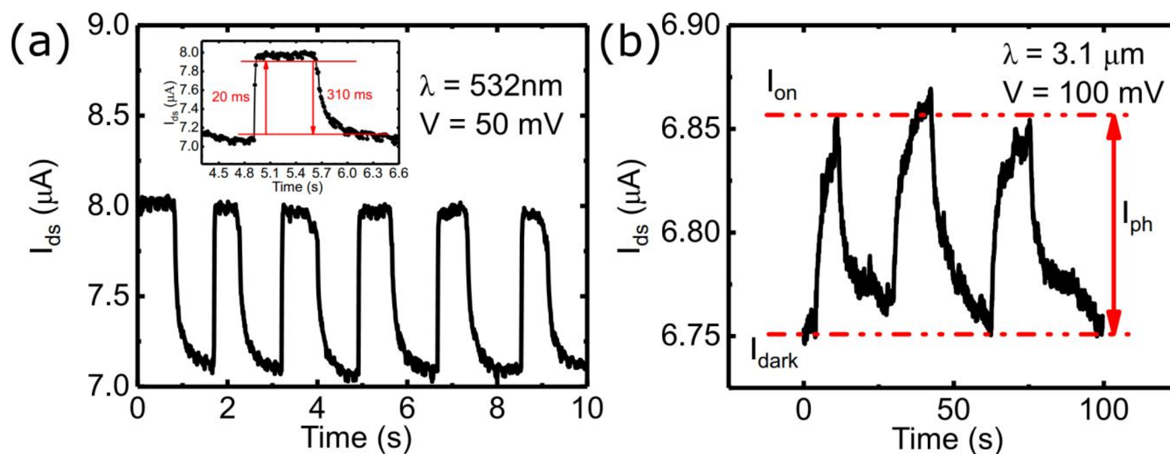

Figure 4. (a) Response to laser pulses with 532 nm wavelength. The rising and falling time is defined in the main text. (b) Response to MIR laser pulses with 3.1 μm wave length.

The band gap values of NST measured by STS and transport indicated that NST devices should have MIR responses. To test its optoelectronic property, we first used 532 nm laser pulses to characterize the NST FETs as shown in Figure 4a. With a source-drain bias of 50 mV, a gate voltage of 0 V and a 310-μW laser, the device showed ~ 1 μA of photocurrent and fast response. We defined the rising and falling times as the time span between 90% and 10% of the total photocurrent, which gave a rising edge of 20 ms and a decaying edge of 310 ms. We note that the dark current was high (~ 7 μA) due to the intrinsic heavy p type doping. Response to MIR wavelength (3.1 μm) was also measured as shown in Figure 4b, with a laser power of ~160 nW. The photocurrent was approximately 100 nA, which gave a responsivity of 0.66 A W^{-1}, much larger than the responsivity of bAP.[4] These results demonstrated the potential of NST for MIR detection.

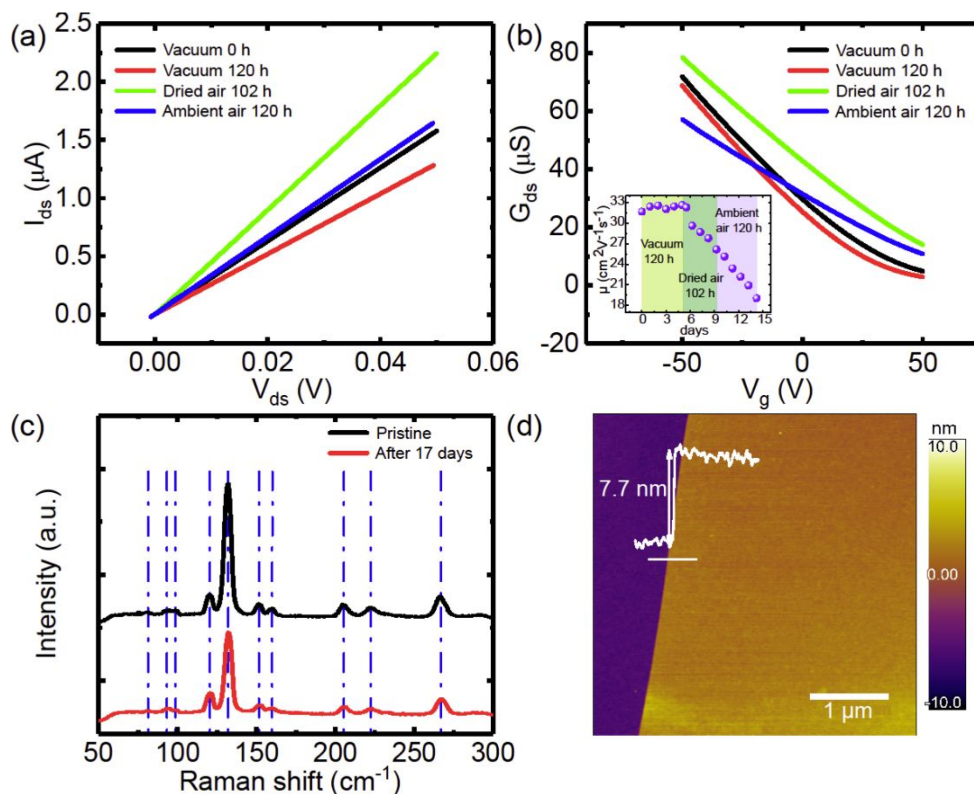

Figure 5. (a) I_{ds} *versus* V_{ds} under different test conditions. (b) Transfer curves show the slight degradation of mobility after the device was exposed to ambient air for 120 hours. Inset: the day-to-day variation of the device mobility. (c) Raman spectra taken before and after the transport measurements shown in (a) and (b). (d) AFM image of the channel after the transport measurements showing the smooth intact surface.

The ambipolar transport and MIR response have shown the application potential of NST. Stability is another important property that should be examined, as it has always been a substantial challenge for narrow bandgap semiconductors, such as bP and bAP.[4,12] These materials tend to react quickly with oxygen and water moisture in air and degrade completely in the time scale of minutes to several hours.[27] Exfoliations of these materials are usually done in

1
2
3
4
5
6
7
8
9
10
11
12
13
14
15
16
17
18
19
20
21
22
23
24
25
26
27
28
29
30
31
32
33
34
35
36
37
38
39
40
41
42
43
44
45
46
47
48
49
50
51
52
53
54
55
56
57
58
59
60

glove boxes with water and oxygen contents less than 1 ppm. Special care during device fabrication and various encapsulation techniques are needed to protect these materials,[4,13,23,28] which brings in extra difficulties and complexities. However, NST showed resistance to ambient conditions. Exfoliation and inspection were all carried out in air. As shown in the transport data in Figure 5a and 5b, when a fabricated device was stored in vacuum for 120 hours, the mobility increased slightly (from black to red curve), due to the desorption of surface contaminant. When exposed to dried air for another 102 hours, mobility was slightly decreased with an increase of conductance (green curve), presumably due to the mild oxidation effect from the air. When the device was stored in air with 40% relative humidity for another 120 hours, the device still showed good transport behavior (blue curve), with 40% reduction of its mobility. In the inset of Figure 5b, day-to-day variation of the mobility was monitored and the numerical values are presented in the SI. After exposure to air, the mobility decreased linearly without obvious change of speed when the air was switched from dry to ambient air with moisture, which indicated the key role of oxygen instead of water. As a comparison, bP and bAP devices usually completely lost their electrical conductivity after a few hours exposure to moisture air.[28] Raman spectra of the same device before and after measurements also revealed the stability of NST (Figure 5 c). All the peaks retained their positions and line profiles, and no new peaks could be seen. The decrease in intensity can be ascribed to the surface oxidization of NST. The AFM image (Figure 5d) of the channel after all the characterizations shows the cleanness and flatness of the flake, compared with the chemically corroded rough surface of bP and bAP.[4,12,29] A similar stability can be seen on another device in Figure S6 of the SI.

CONCLUSIONS

In conclusion, we have explored the layered material Nb_2SiTe_4 as a 2D narrow-gap semiconductor. Ambipolar transport with respectable mobility and comparable electron-hole injection indicate its outstanding electronic property. Good responsivity to MIR wavelength demonstrates the great potential for optoelectronic applications. In addition to these characteristics, its superior stability renders Nb_2SiTe_4 a special position among all the narrow-gap 2D materials, which warrants its further exploration.

METHODS

Crystal growth: Nb (99.95%, Aladdin Chemicals), Si (99.999%, Aladdin Chemicals), and Te (99.99%, Aladdin Chemicals) powders in a molar ratio of 1:2:8 were mixed using a mortar for 20 minutes and placed into an alumina crucible. The extra Si and Te were used as the flux for reducing the melting temperature of Nb. The crucible was sealed into a quartz tube in vacuum of 10^{-4} Pa and then heated in a high-temperature well-type furnace up to 1150 °C in 15 hours. After reaction at this temperature for 5 hours, the assembly was slowly cooled down to 750 °C at a rate of 1 °C /h and stayed at 750 °C for 15 hours. The excess Si and Te were quickly removed from the alumina crucible at this temperature in a centrifuge without breaking the vacuum. Then, the quartz tube was cooled down to room temperature in air. Thin pieces of black Nb_2SiTe_4 flakes with metallic luster were obtained in the alumina crucible.

STM and STS: The STM experiments were carried out in the Omicron LT-Qpuls-STM with tungsten tip calibrated on Ag(111) surface. To get clean surface, the NST bulk sample was exfoliated in ultrahigh vacuum chamber with the base pressure $< 10^{-9}$ mbar and then transferred to STM chamber to start the scanning with the base pressure of 10^{-11} mbar and temperature of 77 K.

1
2
3
4
5
6
7
8
9
10
11
12
13
14
15
16
17
18
19
20
21
22
23
24
25
26
27
28
29
30
31
32
33
34
35
36
37
38
39
40
41
42
43
44
45
46
47
48
49
50
51
52
53
54
55
56
57
58
59
60

Device fabrication and transport measurements: All the FET devices in this study were started with NST exfoliation on highly doped silicon wafer covered with 300 nm SiO_2. The electron beam lithography was used to design the contacts. Thermal evaporation of electrode metals (10 nm Ti and 40 nm Au) with lift off method was used to deposit the contacts. Then, the devices were ready for transport measurement, which was carried out in a Janis ST-500 probe station under vacuum. Keithley source meters 2612B provided the source-drain voltage and back gate voltage while measuring the current.

XRD: Powder X-ray diffraction was performed on Nb_2SiTe_4 single crystals aligned along the (001) plane, using a D8 Venture Bruker at room temperature. A Cu kα source (1.5418 Å) was used.

Raman: A custom made micro Raman system with ANDOR SR-500i-D2-R spectrometer and 1800 grooves per mm grating was used. The incident laser wavelength was 532 nm.

AFM: All the AFM images were obtained using AFM (Oxford, Cypher S) under ambient conditions.

ASSOCIATED CONTENT

Supporting Information.

The Supporting Information is available free of charge on the ACS Publications website at DOI: Additional information showing more 3D views of the crystal from different angles, Raman spectra of different NST flakes, UPS measurement to obtain the NST work function, the transport properties of other few-layer NST FETs, the AFM image of the ambipolar device, the stability test of another NST device and the table of mobility values corresponding to Figure 5b.

1
2
3
4
5
6
7
8
9
10
11
12
13
14
15
16
17
18
19
20
21
22
23
24
25
26
27
28
29
30
31
32
33
34
35
36
37
38
39
40
41
42
43
44
45
46
47
48
49
50
51
52
53
54
55
56
57
58
59
60

AUTHOR INFORMATION

Corresponding Authors

*xuejm@shanghaitech.edu.cn, wdhu@mail.sitp.ac.cn, guoyf@shanghaitech.edu.cn

Author Contributions

The manuscript was written through contributions of all authors. All authors have given approval to the final version of the manuscript. ‖These authors contributed equally.

ACKNOWLEDGMENT

We thank Prof. B. Chen for the initial help with the MIR measurements. The device fabrication was supported by the Centre for High-resolution Electron Microscopy (CℏEM), SPST, ShanghaiTech University under contract No. EM02161943. Drs. N. Yu, X. Wang and Z. Zou helped with the XRD. M. Z., Z.T. and J.X. are supported by the Thousand Talents Project and ShanghaiTech University. W. X. and Y.G. are supported by the Natural Science Foundation of Shanghai (17ZR1443300) and the Shanghai Pujiang Program (17PJ1406200). Y. W., M. L., and W. H. are supported by the National Natural Science Foundation of China (61674157, 11734016).

REFERENCES

(1). Guo, Q.; Pospischil, A.; Bhuiyan, M.; Jiang, H.; Tian, H.; Farmer, D.; Deng, B.; Li, C.; Han, S. J.; Wang, H.; Xia, Q.; Ma, T. P.; Mueller, T.; Xia, F. Black Phosphorus Mid-Infrared Photodetectors with High Gain. *Nano Lett.* **2016,** *16*, 4648-4655.
(2). Youngblood, N.; Chen, C.; Koester, S. J.; Li, M. Waveguide-Integrated Black Phosphorus Photodetector with High Responsivity and Low Dark Current. *Nat. Photonics* **2015,** *9*, 247-252.
(3). Yuan, H.; Liu, X.; Afshinmanesh, F.; Li, W.; Xu, G.; Sun, J.; Lian, B.; Curto, A. G.; Ye, G.; Hikita, Y.; Shen, Z.; Zhang, S. C.; Chen, X.; Brongersma, M.; Hwang, H. Y.; Cui, Y. Polarization-Sensitive Broadband Photodetector Using a Black Phosphorus Vertical P-N Junction. *Nat. Nanotechnol.* **2015,** *10*, 707-713.

(4). Long, M.; Gao, A.; Wang, P.; Xia, H.; Ott, C.; Pan, C.; Fu, Y.; Liu, E.; Chen, X.; Lu, W.; Nilges, T.; Xu, J.; Wang, X.; Hu, W.; Miao, F. Room Temperature High-Detectivity Mid-Infrared Photodetectors Based on Black Arsenic Phosphorus. *Sci. Adv.* **2017,** *3*, e1700589.
(5). Liu, B.; Kopf, M.; Abbas, A. N.; Wang, X.; Guo, Q.; Jia, Y.; Xia, F.; Weihrich, R.; Bachhuber, F.; Pielnhofer, F.; Wang, H.; Dhall, R.; Cronin, S. B.; Ge, M.; Fang, X.; Nilges, T.; Zhou, C. Black Arsenic-Phosphorus: Layered Anisotropic Infrared Semiconductors with Highly Tunable Compositions and Properties. *Adv. Mater.* **2015,** *27*, 4423-4429.
(6). Ye, L.; Li, H.; Chen, Z.; Xu, J. Near-Infrared Photodetector Based on MoS2/Black Phosphorus Heterojunction. *ACS Photonics* **2016,** *3*, 692-699.
(7). Shim, J.; Oh, S.; Kang, D. H.; Jo, S. H.; Ali, M. H.; Choi, W. Y.; Heo, K.; Jeon, J.; Lee, S.; Kim, M.; Song, Y. J.; Park, J. H. Phosphorene/Rhenium Disulfide Heterojunction-Based Negative Differential Resistance Device for Multi-Valued Logic. *Nat. Commun.* **2016,** *7*, 13413.
(8). Li, L.; Yu, Y.; Ye, G. J.; Ge, Q.; Ou, X.; Wu, H.; Feng, D.; Chen, X. H.; Zhang, Y. Black Phosphorus Field-Effect Transistors. *Nat. Nanotechnol.* **2014,** *9*, 372-377.
(9). Han, C.; Hu, Z.; Gomes, L. C.; Bao, Y.; Carvalho, A.; Tan, S. J. R.; Lei, B.; Xiang, D.; Wu, J.; Qi, D.; Wang, L.; Huo, F.; Huang, W.; Loh, K. P.; Chen, W. Surface Functionalization of Black Phosphorus *via* Potassium toward High-Performance Complementary Devices. *Nano Lett.* **2017,** *17*, 4122-4129.
(10). Tian, H.; Deng, B.; Chin, M. L.; Yan, X.; Jiang, H.; Han, S. J.; Sun, V.; Xia, Q.; Dubey, M.; Xia, F.; Wang, H. A Dynamically Reconfigurable Ambipolar Black Phosphorus Memory Device. *ACS Nano* **2016,** *10*, 10428-10435.
(11). Low, T.; Chaves, A.; Caldwell, J. D.; Kumar, A.; Fang, N. X.; Avouris, P.; Heinz, T. F.; Guinea, F.; Martin-Moreno, L.; Koppens, F. Polaritons in Layered Two-Dimensional Materials. *Nat. Mater.* **2017,** *16*, 182-194.
(12). Guo, Z.; Chen, S.; Wang, Z.; Yang, Z.; Liu, F.; Xu, Y.; Wang, J.; Yi, Y.; Zhang, H.; Liao, L.; Chu, P. K.; Yu, X. F. Metal-Ion-Modified Black Phosphorus with Enhanced Stability and Transistor Performance. *Adv. Mater.* **2017,** *29*, 1703811.
(13). Wan, B.; Yang, B.; Wang, Y.; Zhang, J.; Zeng, Z.; Liu, Z.; Wang, W. Enhanced Stability of Black Phosphorus Field-Effect Transistors with SiO_2 Passivation. *Nanotechnology* **2015,** *26*, 435702.
(14). Tremel, W.; Kleinke, H.; Derstroff, V.; Reisner, C. Transition Metal Chalcogenides: New Views on An Old Topic. *J. Alloys Compd.* **1995,** *219*, 73-82.
(15). Springer Materials. https://materials.springer.com/isp/crystallographic/docs/sd_1414898 (accessed January 8,2019).
(16). Wang, Q. H.; Kalantar-Zadeh, K.; Kis, A.; Coleman, J. N.; Strano, M. S. Electronics and Optoelectronics of Two-Dimensional Transition Metal Dichalcogenides. *Nat. Nanotechnol.* **2012,** *7*, 699-712.
(17). Xi, X.; Berger, H.; Forro, L.; Shan, J.; Mak, K. F. Gate Tuning of Electronic Phase Transitions in Two-Dimensional $NbSe_2$. *Phys. Rev. Lett.* **2016,** *117*, 106801.
(18). Fischer, Ø.; Kugler, M.; Maggio-Aprile, I.; Berthod, C.; Renner, C. Scanning Tunneling Spectroscopy of High-Temperature Superconductors. *Rev. Mod. Phys.* **2007,** *79*, 353-419.
(19). Li, G.; Luican, A.; Andrei, E. Y. Scanning Tunneling Spectroscopy of Graphene on Graphite. *Phys. Rev. Lett.* **2009,** *102*, 176804.
(20). Das, S.; Chen, H. Y.; Penumatcha, A. V.; Appenzeller, J. High Performance Multilayer MoS_2 Transistors with Scandium Contacts. *Nano Lett.* **2013,** *13*, 100-105.

1
2
3
4
5
6
7
8
9
10
11
12
13
14
15
16
17
18
19
20
21
22
23
24
25
26
27
28
29
30
31
32
33
34
35
36
37
38
39
40
41
42
43
44
45
46
47
48
49
50
51
52
53
54
55
56
57
58
59
60

(21). Zhou, X.; Zhang, Q.; Gan, L.; Li, H.; Xiong, J.; Zhai, T. Booming Development of Group IV-VI Semiconductors: Fresh Blood of 2D Family. *Adv. Sci.* **2016,** *3*, 1600177.
(22). Manzeli, S.; Ovchinnikov, D.; Pasquier, D.; Yazyev, O. V.; Kis, A. 2D Transition Metal Dichalcogenides. *Nat. Rev. Mater.* **2017,** *2*, 17033.
(23). Li, L.; Yang, F.; Ye, G. J.; Zhang, Z.; Zhu, Z.; Lou, W.; Zhou, X.; Li, L.; Watanabe, K.; Taniguchi, T.; Chang, K.; Wang, Y.; Chen, X. H.; Zhang, Y. Quantum Hall Effect in Black Phosphorus Two-Dimensional Electron System. *Nat. Nanotechnol.* **2016,** *11*, 593-597.
(24). Hao, Y.; Wang, L.; Liu, Y.; Chen, H.; Wang, X.; Tan, C.; Nie, S.; Suk, J. W.; Jiang, T.; Liang, T.; Xiao, J.; Ye, W.; Dean, C. R.; Yakobson, B. I.; McCarty, K. F.; Kim, P.; Hone, J.; Colombo, L.; Ruoff, R. S. Oxygen-Activated Growth and Bandgap Tunability of Large Single-Crystal Bilayer Graphene. *Nat. Nanotechnol.* **2016,** *11*, 426-431.
(25). Chu, T.; Ilatikhameneh, H.; Klimeck, G.; Rahman, R.; Chen, Z. Electrically Tunable Bandgaps in Bilayer MoS_2. *Nano Lett.* **2015,** *15*, 8000-8007.
(26). Sze, S. M.; Ng, K. K. *Physics of Semiconductor Devices*. Wiley: Hoboken, New Jersey, UAS, 2007; pp 314-315.
(27). Castellanos-Gomez, A.; Vicarelli, L.; Prada, E.; Island, J. O.; Narasimha-Acharya, K. L.; Blanter, S. I.; Groenendijk, D. J.; Buscema, M.; Steele, G. A.; Alvarez, J. V.; Zandbergen, H. W.; Palacios, J. J.; van der Zant, H. S. J. Isolation and Characterization of Few-Layer Black Phosphorus. *2D Mater.* **2014,** *1*, 025001.
(28). Wood, J. D.; Wells, S. A.; Jariwala, D.; Chen, K. S.; Cho, E.; Sangwan, V. K.; Liu, X.; Lauhon, L. J.; Marks, T. J.; Hersam, M. C. Effective Passivation of Exfoliated Black Phosphorus Transistors Against Ambient Degradation. *Nano Lett.* **2014,** *14*, 6964-6970.
(29). Abellan, G.; Wild, S.; Lloret, V.; Scheuschner, N.; Gillen, R.; Mundloch, U.; Maultzsch, J.; Varela, M.; Hauke, F.; Hirsch, A. Fundamental Insights into the Degradation and Stabilization of Thin Layer Black Phosphorus. *J. Am. Chem. Soc.* **2017,** *139*, 10432-10440.

1
2
3
4
5
6
7
8
9
10
11
12
13
14
15
16
17
18
19
20
21
22
23
24
25
26
27
28
29
30
31
32
33
34
35
36
37
38
39
40
41
42
43
44
45
46
47
48
49
50
51
52
53
54
55
56
57
58
59
60

For Table of Contents Only